BBA - Bioenergetics 1867 (2026) 149598

Contents lists available at ScienceDirect

BBA - Bioenergetics

journal homepage: www.elsevier.com/locate/bbabio

Cryo-EM structure of photosystem II D1-V185T mutant from *Thermosynechococcus vestitus*

Haowei Jiang [a], Yoshiki Nakajima [a], Fusamichi Akita [a], Hongjie Li [b], Koji Kato [a], Miwa Sugiura [c], Jian-Ren Shen [a,*]

[a] *Research Institute for Interdisciplinary Science, Advanced Research Field and Graduate School of Environmental, Life, Natural Science and Technology, Okayama University, Okayama, 700-8530, Japan*

[b] *Center for Transformative Science, School of Life Science and Technology and Shanghai Clinical Research and Trial Center, ShanghaiTech University, Shanghai, 201210, China*

[c] *Proteo-Science Research Center, Ehime University, Bunkyo-cho, Matsuyama, Ehime, 790-8577, Japan*

ARTICLE INFO

Keywords:
Photosystem II
Oxygen-evolving complex
Water-oxidation
Structure
Mutant
Cryo-EM
Thermosynechococcus vestitus

ABSTRACT

Photosystem II (PSII) catalyzes water oxidation into electrons, protons and dioxygen at its catalytic center, a Mn_4CaO_5 cluster, utilizing light energy. An amino acid residue D1-V185 in the D1 protein is located close to the Mn_4CaO_5 cluster, and plays a critical role in its catalytic function. In this research we purified PSII dimers from a D1-V185T mutant of *Thermosynechococcus vestitus* and analyzed its structure using low-damage cryo-electron microscopy (cryo-EM) at a resolution of 1.88 Å. The results revealed the presence of multi-conformations at the mutation site. Unlike the wild-type valine, which does not allow water molecules to be able to form hydrogen-bonds with it, both conformations of the mutant formed hydrogen bonds with nearby water molecules, which leads to rearrangement of the hydrogen bond networks in the O1 and Cl-1 channels. In conformation-A, the mutated Thr residue forms a hydrogen bond with a water molecule W6, which creates a new channel that by-passes the original O1 channel. Due to the hydrophilic OH group of Thr, the side-chain of D1-Glu189 was attracted and shifted toward the mutant Thr residue. In conformation-B, it forms a hydrogen bond with a water molecule W9 in the Cl-1 channel, bringing W9 closer and thereby disrupting the hydrogen bond network of the Cl-1 channel. In addition, multi-conformations of D2-K317, which is a ligand of Cl-1, were found in the mutant. These changes alter the environment surrounding the Cl-1 ion and Mn_4CaO_5, thereby affecting the PSII water-oxidation activity.

1. Introduction

Photosystem II (PSII) captures solar energy and uses it to split water into protons, electrons, and dioxygen, providing the energy and molecular oxygen required for sustaining almost all life forms in the biosphere [1,2]. The reaction of water oxidation to produce molecular oxygen proceeds through five states referred to as the S_i-states (with $i = 0$–4), which represent sequential steps of charge accumulation during water splitting [3]. During one catalytic cycle, PSII oxidizes two water molecules, releasing four protons and four electrons. While electrons are released in every step of the S-state transition, protons are released in a pattern of 1:0:1:2 during the $S_0 \rightarrow S_1 \rightarrow S_2 \rightarrow S_3 \rightarrow (S_4) \rightarrow S_0$ transitions [4,5].

The catalytic center for water oxidation is a Mn_4CaO_5 cluster bound to the lumenal side of PSII, which is coordinated by seven amino acid residues from the D1 and CP43 subunits, as well as four water molecules (W1–W4) [6,7]. The Mn_4CaO_5 cluster is associated with three channels that are proposed to facilitate the transport of substrate water molecules into the reaction site and/or protons out to the lumen. These channels are known as the O1 channel, O4 channel and Cl − 1 channel (Fig. 1) [8–12]. All these channels are connected by hydrogen bonds among amino acid residues and water molecules that are located in the channels, and ultimately exit to the lumenal surface. The O1 and O4 channels refer to hydrogen-bond networks that start or terminate at the O1 and O4 atoms, two oxo-bridged oxygen atoms forming the Mn_4CaO_5 cluster, respectively. Among them, the O1 channel is thought to serve as a pathway for substrate water entry, and the observed flipping of CP43-V410 during the S-state cycle may indicate its role as a gate for water

* Corresponding author.
E-mail address: shen@okayama-u.ac.jp (J.-R. Shen).

https://doi.org/10.1016/j.bbabio.2026.149598
Received 2 April 2026; Received in revised form 18 June 2026; Accepted 19 June 2026
Available online 22 June 2026

molecules to come in through this channel [9,13–15]. The O4 channel has been predicted to function as a proton release pathway, with movements and disappearance of internal water molecules observed during S-state transitions [8,13,16].

On the other hand, the Cl − 1 channel consists of an extended hydrogen-bond network from the Mn_4CaO_5 cluster through the Cl–1 binding site, to the lumenal surface in two branches. Branch A goes through D1-D61 and D1-E65, and branch B goes through D2-K317, PsbO-P159 and PsbO-K160 [1,9,13]. This channel has been proposed to release protons during the S_2-to-S_3 and/or S_3-to-S_0 transitions [13–15]. There may be another channel, Cl–2 channel, that is mediated by the Cl–2 ion in the vicinity of the Mn_4CaO_5 cluster [17], but whether this channel plays a role in the water/proton transport is not clear at present. Given that these channels are all well connected through hydrogen-bond networks, they may have overlapping or cooperative roles in both proton and water transfer.

Efficient water oxidation and oxygen evolution require not only stepwise electron transfer and the accumulation of oxidizing equivalents in the Mn_4CaO_5 cluster [1,2], but also structural dynamics including reorganization of the surrounding hydrogen-bond networks to enable the coordinated transfer and release of protons and water molecules [9,13,15]. Even subtle perturbations in these local structural interactions can markedly retard water oxidation or even abolish photoautotrophic growth [18]. Thus, how PSII maintains and regulates these processes remains a central issue in understanding the mechanism of photosynthetic water oxidation and oxygen evolution.

D1-V185 is a hydrophobic residue located close to the Mn_4CaO_5 cluster [6,7]. It is highly conserved during evolution, and is thought to play an important role in maintaining water-oxidation activity [18]. Indeed, sequence analysis shows a conservation rate of 98.6% among 2920 sequences retrieved from the database (see Materials and methods). If we consider possible sequence errors and incomplete sequences, the conservation of this residue should be close to 100%, and no other residues have been found in this position in the known, functional D1 proteins. Mutation of D1-V185 to Pro, Asp, or Trp in *Synechocystis* sp. PCC 6803 has been shown to abolish the oxygen-evolving activity and photoautotrophic growth, although changes to N or T retain part of the oxygen-evolving activity and photoautotrophic growth [18]. Furthermore, the D1-V185N mutation is shown to perturb the extensive network of hydrogen bonds that extends from Y_Z to D1-D61, and alter

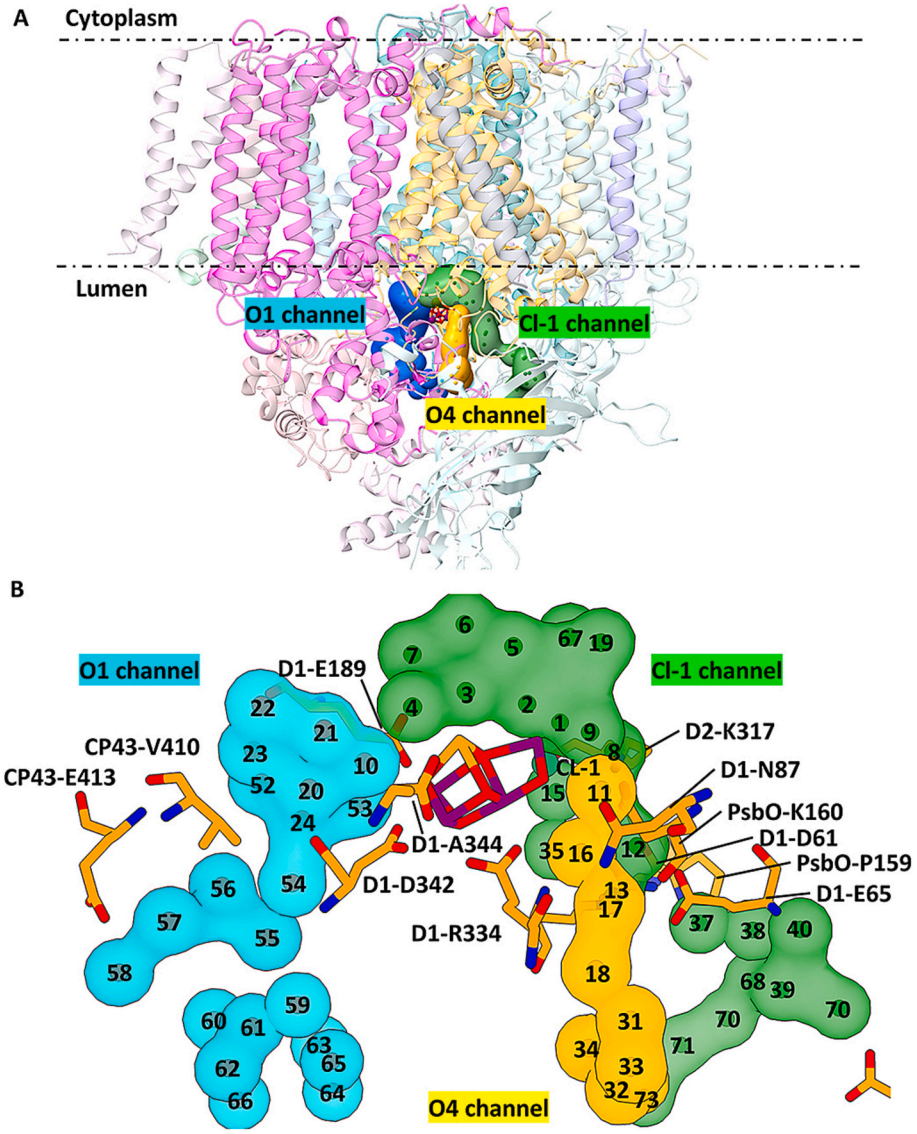

Fig. 1. An overview of the PSII structure and main channels connecting the Mn_4CaO_5 cluster to the lumenal surface. (A) The structure of PSII, displayed in a cartoon representation with different colors for various subunits and the three channels (O1, O4 and Cl–1 channels) (3WU2) [6]. (B) Water molecules in each channel and their numbering (their correspondences to the PDB file numbering are listed in Supplementary Table 5).

the environment of the water molecule whose bending mode vanishes during the S_2 to S_3 transition [19]. This mutation also affects the exchange rate of W_s in the S_1 and S_2 states, as well as both W_s and W_f in the S_3 state, and results in the disappearance of the split electron paramagnetic resonance (EPR) signal in the S_3-state [20]. These results suggest that the N185 residue stabilizes the binding of an additional water-derived ligand at the Mn1 site of the Mn_4CaO_5 cluster via hydrogen bonding [20]. Very recently, the structure of a D1-V185N mutant in *Synechocystis* sp. PCC 6803 was analyzed by cryo-electron microscopy (cryo-EM), which indeed shows perturbations to the Cl-1 mediated hydrogen-bonding network [21]. In the structure of the mutant, N185 orients away from the oxygen-evolving complex (OEC) and donates a hydrogen-bond to Cl–1, a conserved chloride ion close to OEC [21]. Furthermore, the D2-K317 side chain shows an alternative D2-E312-facing conformation in the Cl–1 water channel, which is consistent with recent models for proton transfer. These changes may retard the proton egress during water oxidation, thereby lowering the oxygen-evolving activity.

On the other hand, a V185T mutant was constructed in a thermophilic cyanobacterium *Thermosynechococcus vestitus* (formerly *T. elongatus*) and characterized [22]. In this mutant, a high proportion of the S_2^{HS} configuration is observed. While a proton is likely released in the $S_1 \rightarrow S_2^{HS}$ transition in the wild-type PSII, no proton release is observed in this transition in the V185T mutant [22]. The $S_3 \rightarrow S_0$ transition was dramatically slowed down in the V185T mutant, which may indicate less efficient relaxation of the hydrogen-bond network and/or changes in the protein environment [22]. Indeed, it was shown recently that both V185T and V185N mutants significantly affect proton release during the S_3-to-S_0 transition, suggesting the disruption of the hydrogen-bonding interactions necessary for release of protons from the substrate water [23]. The introduction of such non-native hydrogen bonds may perturb the normal arrangement of amino acid residues and water molecules in the Cl-1 channel, thereby affecting the native hydrogen-bond network in this channel. This disruption in proton transfer was correlated with a slower water exchange in the S_3-state, likely due to non-native hydrogen bonds introduced by the Thr or Asn side chains at position 185 [23].

In this study, we determined the structure of PSII purified from the D1-V185T mutant from *T. vestitus* by cryo-EM. Given that electron beams used in cryo-EM can damage the PSII structure, we selected only the first two frames from the cryo-EM movies to minimize beam-induced damage. The use of these frames gives rise to minimization of radiation damage and results in an intact PSII structure [24]. Our results showed two conformations for the mutated Thr residue, both of which have altered interactions with the nearby water molecules in the Cl–1 channel. Among them, at least one conformation may be responsible for the impairment in the proton release.

2. Results

2.1. Overall structure

PSII dimers were isolated from the D1-V185T mutant, whose oxygen-evolving activity was measured to be 581 ± 44 μmoles O_2 (mg Chl)$^{-1}$ h^{-1}. This activity is only 15% of the PSII dimer isolated from the wild-type. The isolated PSII dimer particles were visualized by cryo-EM (see Materials and methods). After picking up the particles from 18,027 movies with CryoSPARC [25] followed by polishing and 3D refinement with RELION [26], we obtained a global resolution of 1.75 Å for the whole structure of the mutant PSII (Supplementary Fig. 1). However, we observed unrealistic distances within the Mn_4CaO_5 cluster and damage to several amino acid residues, similar to those reported by Kato et al. [24]. This indicates that the PSII protein structure experienced significant electron beam damage when including all frames with a total dose of 50 $e^-/Å^2$ (Supplementary Table 1), which may potentially lead to misinterpretations of the effects of the mutation. To address this issue and minimize such damage as much as possible, we employed the RELION Polish method [27] to select the first two frames only for structural analysis, which gives rise to a dose of around 2 $e^-/Å^2$ and a map with a resolution of 1.88 Å at FSC = 0.143 [28] (Supplementary Figs. 1 and 2). Although the nominal resolution was slightly lower than that of the all-frame reconstruction, this low-dose map showed markedly reduced radiation damage and provided a more reliable basis for structural interpretation of the Mn_4CaO_5 cluster and its surrounding environment.

This resolution theoretically allows for proton modeling with ServalCat [29,30]. However, the number of observable protons was limited. Consequently, we decided not to calculate hydrogen atom positions. In the local resolution map, we observed a resolution of approximately 1.6 Å near the central OEC region (Fig. 2A, D). This level of detail is sufficient to clearly resolve amino acid side chain atoms, positions of water molecules, and components of the Mn_4CaO_5 cluster, with minimal electron beam damage (Fig. 2). To minimize the influence of noise inherent to cryo-EM maps, the map level that has almost no signals in the nearly noise-free outer regions of the protein (σ = 1.7 rmsd) was used as a reference for final model building.

Our structural analysis revealed no significant changes in the distances between O5 and the Mn atoms of the Mn_4CaO_5 cluster [5,6,12,31], although slightly elongated distances are still observed for some of the bond distances within the Mn_4CaO_5 cluster (Fig. 2D), which may be caused by residual radiation damage. At the D1-V185T mutation site, we identified two major, distinct conformations of the D1-185T side chain in the same PSII structure (Fig. 2B, C). The first conformation, with the side chain of T185 oriented toward a water molecule W6, forms a stable hydrogen bond with W6 and is designated conformation-A, which appears to stabilize W6 via the hydrogen bond (Fig. 2B). In contrast, the second conformation, where the side chain of T185 is oriented toward W9, establishes a hydrogen bond with W9 and is called conformation-B (Fig. 2C). These two conformations exhibit distinct hydrogen-bonding patterns with nearby water molecules, suggesting potential roles in modulating the S-state transitions of the OEC and/or the proton transfer pathway. We describe the structures of these two conformations in detail below.

2.2. Conformation-A

We observed that in conformation-A of the D1-V185T mutant, the hydroxyl (OH) group of T185 is located within hydrogen-bonding distances of W6, the backbone carbonyl oxygen atoms of D1-N181 and D1-F182, and the backbone amide nitrogen of D1-F186, respectively, suggesting possible hydrogen-bonding or polar interactions among these groups (Fig. 2B). Among these groups, the distance between D1-185T and W6 is especially short (2.54 Å), suggesting a strong hydrogen bond between them. Because the positions of hydrogen atoms cannot be accurately determined in the present cryo-EM map, we evaluated these possible hydrogen bonds based not only on distances but also on heavy-atom-based angle measurements. Conversely, in the wild-type there are no such hydrogen bonds formed, because the V side chain cannot form hydrogen bonds with the surrounding water molecules and hydrophilic residues. By comparison, in conformation-B, the OH group of T185 forms only two weaker hydrogen bonds—with W9 and the backbone C═O of D1-N181 (Fig. 2C). Based on both the distances and the number of hydrogen bonds to the neighboring residues or water molecules, we conclude that conformation-A is more stable than conformation-B in the S_1 state. However, the occupancy calculations by Phenix based on the cryo-EM map showed that conformation-A and conformation-B have nearly identical occupancies, contradicting the inference that conformation-A is more stable. This discrepancy may indicate that certain factors destabilize conformation-A during the S-state cycle. We will address this issue in the Discussion section.

Compared with the wild-type structure, the B-factors of the OE1 and OE2 atoms of D1-E189 are increased in the mutant (Supplementary Table 2), which is more likely attributable to the influence of

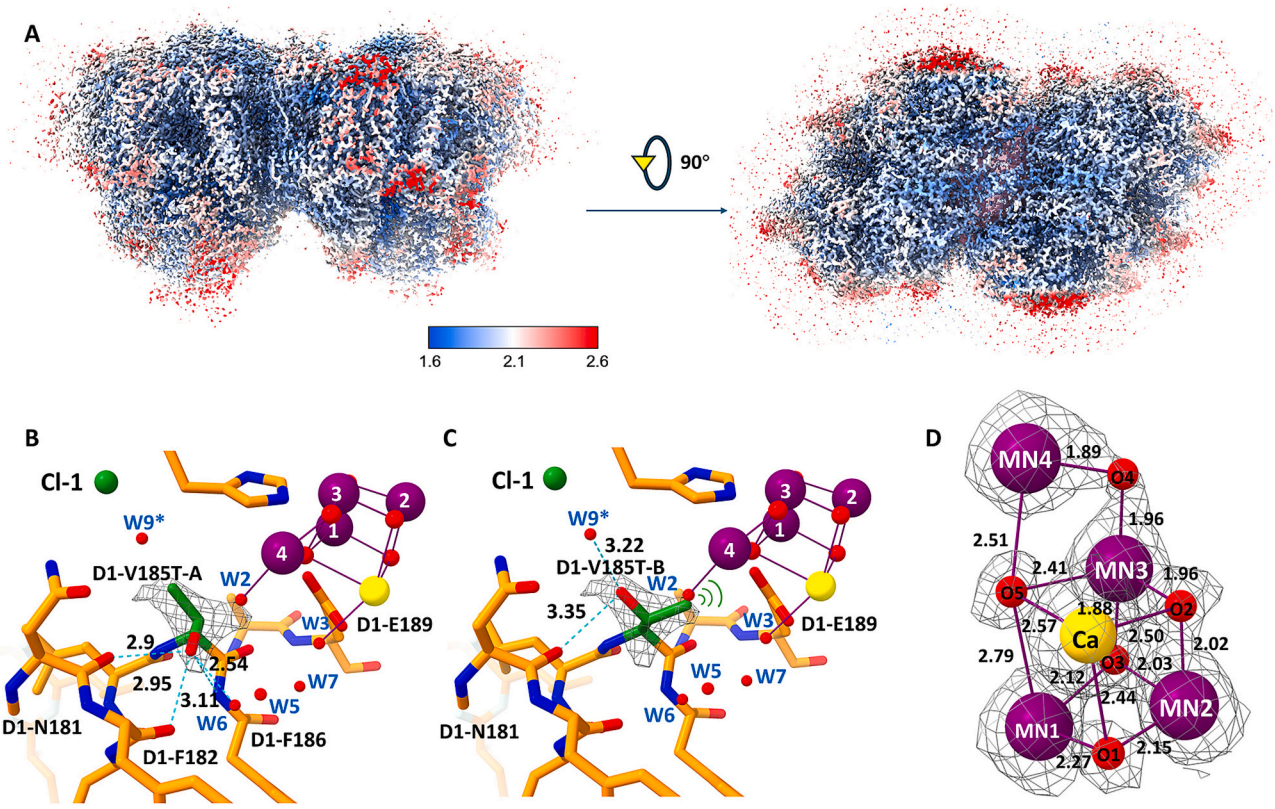

Fig. 2. Local resolution of the cryo-EM map and multi-conformations of PSII D1-V185T. (A) Local resolution map of the mutant PSII generated from frames 1–2, with resolution represented as a gradient from 1.6 Å (blue) to 2.6 Å (red). (B) The structure of D1-V185T conformation-A, highlighting its key features. Numbers in white in panels A and B represent the Mn ion numbering shown in panel D. (C) The structure of D1-V185T conformation-B, illustrating differences in side-chain orientation and interactions compared to conformation-A. (D) The Mn_4CaO_5 cluster of the mutant PSII superimposed with their densities, where purple represents Mn atoms, red represents O atoms, and yellow represents the Ca atom. Cyan dashed lines in panels (B) and (C) depict hydrogen bonds, with the numbers representing interatomic distances (Å). (For interpretation of the references to color in this figure legend, the reader is referred to the web version of this article.)

conformation-A in the mutant structure. In conformation-A, replacement of D1-V185 with T alters the local hydrophobic environment around D1-E189 (Fig. 3A), which allows D1-E189 to shift toward D1-T185. Moreover, the distance of D1-E189-OE2 to O5 is shortened from 3.4 to 3.5 Å in the X-ray and cryo-EM structures of wild-type PSII to 3.22 Å in the mutant (Supplementary Table 3). Additionally, we observed the formation of a new channel calculated by MoleOnline [32], due to the absence of the hydrophobic side chain of D1-V185, which results in alterations in the water molecule pathway (Fig. 3A). In the wild-type structure, the side chain of D1-V185 is hydrophobic and helps direct the O1 channel toward Mn4. However, in the D1-T185-A variant, rotation of the side chain leads to a loss of a corrective function of this side chain, causing the appearance of a new channel which connects the O1 channel with the Cl-1 channel (Fig. 4A).

As shown above (Fig. 3B), the T185 OH group forms a hydrogen bond with W6 in conformation-A. W6 is connected via hydrogen bonds to W5 in the Cl–1 channel and W7, a water molecule connected to Y_Z. These water molecules do not shift their positions significantly in the mutant in comparison with the wild-type. The newly formed hydrogen-bond network, comprising Ca–W3–W7–W6–T185, includes a strong

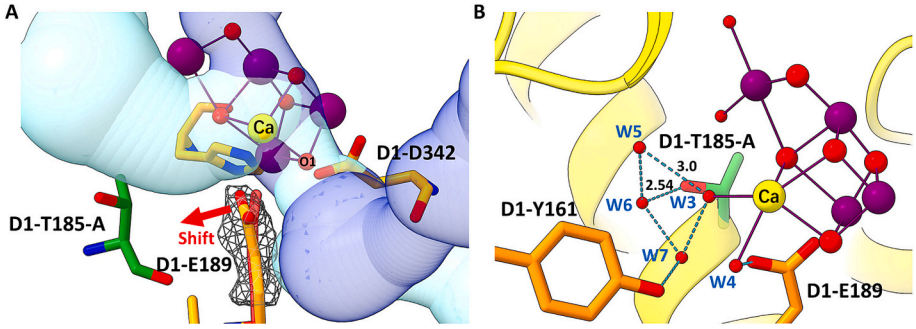

Fig. 3. Effects of conformation-A of the D1-V185T mutant on D1-E189 and the involved hydrogen bonds. (A) Hydrophilic attraction of D1-E189 by D1-T185-A. Black mesh represents the cryo-EM map at rmsd = 1.7, and the red arrow indicates the movement of the side chain of D1-E189. The transparent, red colored D1-E189 depicts its structure in the wild-type PSII (PDB ID: 4ub6) [7], whereas the dark yellow one represents its structure in the mutant. The cyan channel represents the newly appeared water channel calculated using MoleOnline [31], which is connected to the O1 channel. (B) Involvement of D1-T185 in hydrogen bonding in conformation-A, with hydrogen bonds represented as cyan dashed lines. In both panels A and B, the residue of T185 is shown in green, oxygen atoms in red, and nitrogen atoms in blue. (For interpretation of the references to color in this figure legend, the reader is referred to the web version of this article.)

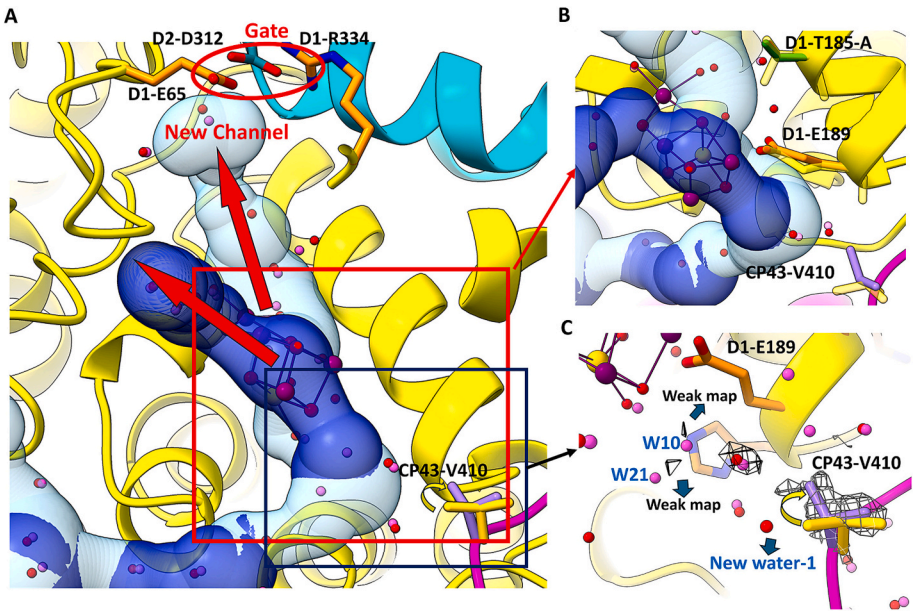

Fig. 4. Structural changes in the O1 water channel, including CP43-V410 and associated water molecules. (A) The water channels were calculated using MoleOnline [31]. The dark blue channel represents the pathway calculated from the wild-type PSII structure (7D1U, 24), while the light-cyan channel corresponds to the pathway calculated for the V185T mutant. D1 is shown in yellow, D2 is shown in dark cyan, and CP43 is shown in medium purple. (B) An enlarged view of the boxed area by red lines in panel A. Yellow marks the positions of D1-V185 and D1-E189 in the wild-type 7D1U structure; the green residue (D1-T185) denotes the conformation-A of the mutant structure, and the orange residue (D1-E189) marks the position of D1-E189 in the D1-V185T mutant. (C) Structure around the CP43-V410 area. The CP43-V410 residue in the wild-type structure (7D1U) is shown in yellow, and in the V185T mutant it is shown in medium purple. The maps are displayed as black solid meshes. The red water molecules represent those observed in the V185T mutant, and the pink water molecules represent those present in the wild-type structure (7D1U). Newly observed water molecules are labeled as "New water". The presence of an unstable region around W10 is represented by a weak density in black mesh. Water molecules newly appeared or became unstable in the V185T mutant are marked with blue arrows. (For interpretation of the references to color in this figure legend, the reader is referred to the web version of this article.)

hydrogen bond (distance <2.7 Å, between D1-T185 and W6), while the distance between W3 and W5 is increased from 2.8 Å in the wild-type to 3.0 Å in the mutant. The addition of a hydrogen bond between T185 and W6 may stabilize the binding of Ca^{2+}, and this rearranged hydrogen-bond network may alter the proton transfer efficiency within the Cl–1 channel, leading to the decrease of the oxygen-evolving activity.

CP43-V410, known as one of the gates for the O1 channel, exhibited a flipping motion in the mutant in the dark-adapted S_1-state, which facilitated the formation of a new water channel in the structure (Fig. 4). In the S_1 state of the wild-type PSII, the CP43-V410 side chain points toward D1-D342 and CP43-L401 [6,7,9,12–14,24]. However, in our structure, the CP43-V410 side chain is deflected toward the opposite direction, pointing toward D1-E189 (Supplementary Fig. 3). This conformational state was previously observed in PSII after two flashes, corresponding to the transition from S_2 to S_3-state, and it has been proposed that this structural change is related to the entry of O6 into the Mn_4CaO_5 cluster [9,13].

Through water channel calculations, we observed that in the wild-type PSII structure (PDB ID: 7D1U) [24], the O1 channel does not connect to the Cl–1 channel, and this configuration is maintained by the hydrophobic nature of both D1-V185 and CP43-V410, which stabilize the proper pathway. However, the V185T mutant leads to changes in the O1 channel, creating a new water channel that connects the O1 and Cl–1 channels as described above (Fig. 4). This new water channel also passes through CP43-V410 due to its flipping in the mutant. Additionally, we observed the disappearance of W10 in the O1 channel, whereas a faint map density appeared near the O1 site, suggesting the possible formation of an unstable water molecule close to O1 (Fig. 4B). These structural changes suggest that alterations in the hydrophobic environment around D1-V185 may influence the O1 and Cl–1 channels, thereby affect the functioning of PSII.

2.3. Conformation-B

In conformation-B, OH group of D1-T185 is rotated toward the Cl–1 ion, forming a weaker hydrogen bond with W9 (Figs. 2C and 5). In the wild-type, W9 is connected to the Cl–1 channel through hydrogen bonds with W2 and W8, which therefore participates in the proton transfer through the Cl–1 channel [9,13,14]. The distance between W2 and W9 is 2.86 Å in the wild-type PSII structure (pdb:3WU2) [6]. However, as shown in Fig. 5A and Supplementary Table 4, W9 shifted toward Cl–1 by 1.40 Å, leading to the elongation of the distance between W2 and W9 to 3.93 Å in the mutant. This distance indicates breakage of the hydrogen bond between them, and thus disruption of the local hydrogen-bond network in the Cl–1 channel. As a ligand of the Cl–1 ion, the distance between W9 and Cl–1 ion is shortened from 3.57 Å in the wild-type to 2.47 Å in the mutant (Fig. 5B and Supplementary Table 4), which is an unusually short distance as a halogen bond. Such a distance is rarely observed, as noted in PDB file conclusion analyses (Fig. 5B) [33]. As the density for W9 is well resolved in the mutant, it appears that W9 is stabilized by this short distance with Cl-1. This unusually short Cl–1–W9 distance suggests a strengthened ion–dipole interaction between Cl–1 and W9, which may stabilize the shifted position of W9 and, at the same time, hinder the local water rearrangements required for efficient proton transfer.

Furthermore, we observed the disappearance of the W12 water molecule near D1-D61 (Fig. 5A). In wild-type, W12 forms hydrogen bonds with D1-D61 and W14, the latter further forms hydrogen bonds with D1-E65, D1-R334, D2-E312 and D2-K317 (Fig. 5B). W12 thus may play an important role in proton transfer along the Cl–1 channel, relaying protons from the Mn_4CaO_5 cluster to the gate region. The disappearance of W12 disrupts the hydrogen bond between D1-D61 and D1-E65, preventing proton transfer from D1-D61 to the gate [15]. Therefore, we propose that the movement of W9, together with the loss of W12, substantially perturbs the hydrogen-bond network of the Cl–1

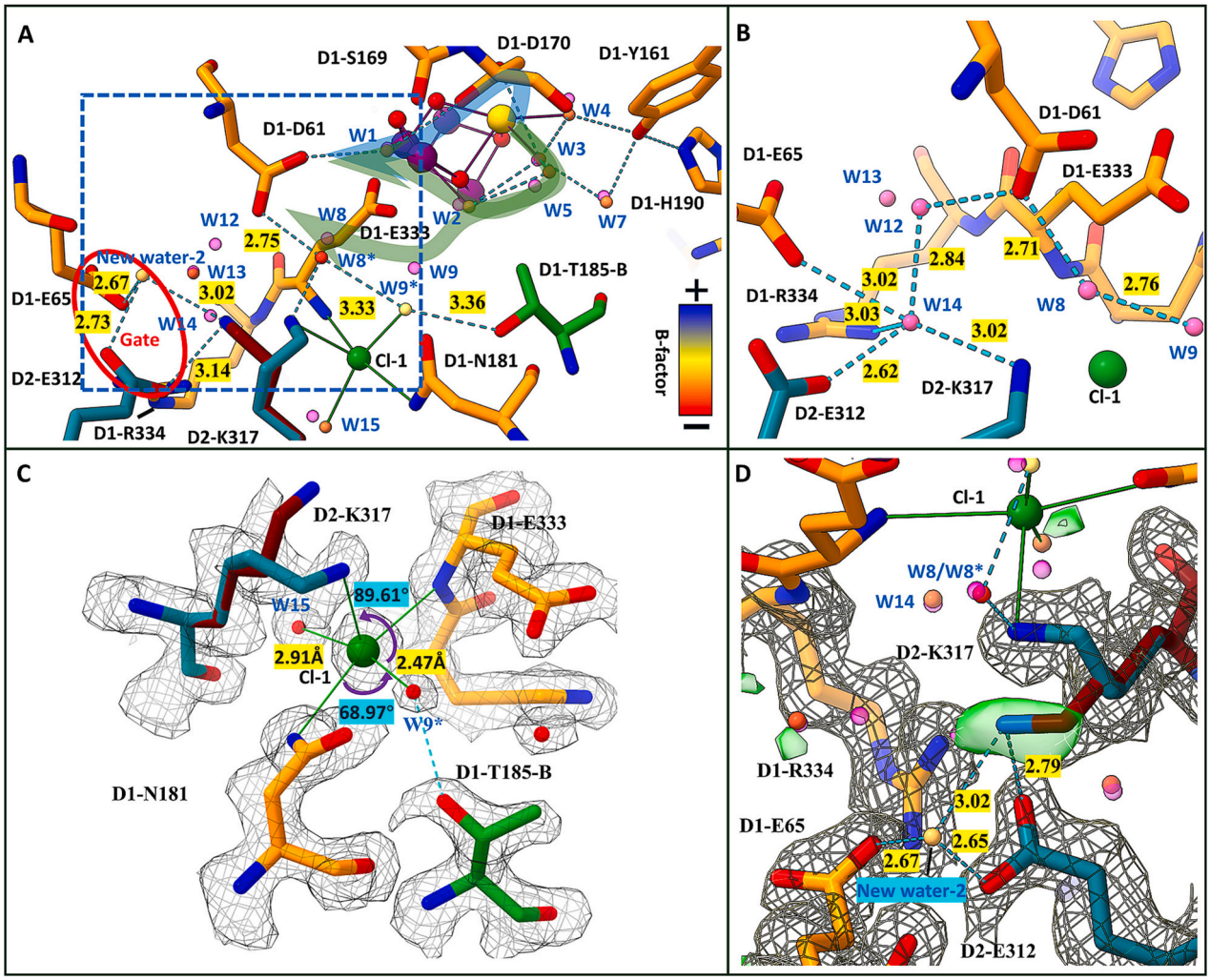

Fig. 5. Cl–1 channel and the Cl–1 ligand environment in conformation-B of the D1-T185 mutant. (A) Structure of the Cl–1 channel region of the mutant PSII, with the water molecules from the wild-type structure (4UB6) [7] depicted as pink spheres, and others from the mutant structure. To distinguish from the wild-type assignment, W9 and W8 in the D1-V185T mutant are labeled W9* and W8*, respectively. The B-factors of water molecules of the D1-V185T mutant structure are represented as a gradient from red (low B-factor) to blue (high B-factor). D1 is shown in orange, D2 is shown in marine, conformation-B of D1-185T is shown in green, and the Cl–1 ion is shown as a green sphere, with its ligands connected by solid green lines. The hydrogen bonds are depicted with greenish dashed lines. The transparent green arrow indicates the breakage of the hydrogen bond between W2 and W9, and the light blue arrow highlights the continued availability of this proton channel. Red cycle indicates the gate area mentioned in the text. (B) Structure of the wild-type PSII (4UB6) in the boxed area in panel A, showing the differences in the hydrogen-bond network. (C) Enlarged view of the Cl–1 binding site of the mutant. The solid green lines connect the Cl-1 atom with its surrounding ligands, and the cyan dashed line depicts the hydrogen bond between D1-T185 and W9*. The angles between the Cl-1 ion and its ligands are shown in purple arrowheads, and the map is visualized as a faded black mesh. The multiple conformations of D2-K317 are shown in reddish and marine, respectively. (D) Superposition of the D2-K317 area with the cryo-EM maps. The black mesh represents Relion map of the V185T mutant, and green density corresponds to the positive $Fo_{(2half\text{-}map)} - Fc_{(model)}$ map, calculated using Servalcat [25] only for the orange conformation and contoured at a level that minimizes noise. Distances of hydrogen bonds are indicated by numbers (in Å) in a yellow background. (For interpretation of the references to color in this figure legend, the reader is referred to the web version of this article.)

channel.

We also observed conformational heterogeneity of D2-K317. When only a single conformation of D2-K317 was assumed during model refinement, a positive Fo–Fc difference density appeared at this site, suggesting the presence of an additional conformation of D2-K317. Such conformational heterogeneity of D2-K317 has been reported in the D1-V185N mutant of *Synechocystis* sp. PCC 6803 [21], where the emergence of this conformation was proposed to result from disruption of the local environment surrounding Cl–1.

Due to the unusually short distance between W9 and Cl–1 (Fig. 5A), D2-K317 may have been prevented from forming a stable salt bridge with the Cl–1 ion. This altered interaction may facilitate the formation and stabilization of a second conformation of D2-K317, which is oriented away from the Cl–1 ion and hence does not ligate to the Cl–1 ion. Meanwhile, owing to the low electron-dose data acquisition and the presence of a new water molecule "New water-2", D2-E312 and D1-E65 exhibit more well-defined electron densities. As a result, we are able to resolve the density for D1-E65 and D2-E312 clearly and to build reliable structural models for these residues. Based on the refined model, the second conformation of K317 forms hydrogen bonds with D2-E312 and New water-2 with distances of 2.79 Å and 3.02 Å, respectively (Fig. 5C). These observations indicate that changes in the ligand environment of the Cl–1 ion can remodel the hydrogen bond network involving D1-E65 and D2-E312.

Disruption of the Cl–1 channel may also impact another potential proton transfer pathway, the O4 channel. From the structural analysis, we observed that water molecules in the O4 channel underwent noticeable rearrangements. The five-water cluster at the outer side of the

O4 channel has been proposed to facilitate Grotthuss-type proton transfer, which is important for proton movement [9,34]. We observed the disappearance of W34 in the O4 channel, and a large shift of the position of W32. Furthermore, the distance between W31 and W33 is decreased from 3.16 Å in the wild-type to 2.53 Å in the mutant, and W31 became highly unstable and could only be detected under conditions of low sigma thresholds [Fig. 6]. This situation resembles the 1F structure observed by XFEL [9]. Since no proton release is detected in the S_1-S_2 transition in the wild-type PSII, the unusually short distance has been interpreted as possibly reflecting proton retention, which is already observed in the mutant PSII in the dark.

3. Discussion

In the D1-V185T mutant, the oxygen-evolving activity of purified PSII was decreased to approximately 15% of the wild-type PSII despite the intact subunit composition. In the present study, several structural changes were observed between the mutant and wild-type PSII in the S_1 state. During cryo-EM single-particle analysis, all maps and data represent averaged conformations, with the occupancy calculation suggesting that each class of the protein particles corresponds to a single conformation [35,36]. We found two conformations of the D1-T185 residue; they are named conformation-A and conformation-B, respectively. The occupancies of conformation-A and conformation-B are both close to 50%. However, a detailed examination of the structures showed that conformation-A may be more stable than conformation-B, but the occupancies of the two structures are 1:1, suggesting that conformation-B may be stabilized by an unknown factor. Conformation-A is characterized by a hydrogen bond with W6 and the absence of a hydrophobic environment near D1-E189. In contrast, conformation-B brings W9 closer, disrupts the W2-W9 hydrogen bond, and leads to a loss of W12, thereby altering the Cl-1 proton channel [9,13,15,37]. We propose that in conformation-A, the side chain of Thr introduces a hydroxyl group (OH) that interacts with the proton transfer pathway, while in the wild-type structure, the methyl group (CH_3) at the same position maintains a hydrophobic environment. The number of hydrogen bonds is generally indicative of the structural stability. However, in conformation-A, D1-T185 contains four short polar contacts (Fig. 2B), whereas in conformation-B, it contains only two, yet the occupancy of the two conformations is similar. This may be because W6 is a water molecule within the proton transfer channel, and its connection to D1-T185 suggests that a proton may have been transferred to D1-T185, potentially inducing a rotation of the more stable conformation-A into conformation-B.

In previous studies, W10 instability and E189 shift were observed in the wild-type PSII following the second flash, indicating the entry of O6 or O6* into the Mn_4CaO_5 cluster during the S_2-to-S_3 transition [13]. In the S_1-state structure of our mutant, we observed W10 instability, E189 shift, and the opening of CP43-V410 gate similarly, relative to the wild-type PSII structure. When O6* enters, it initially binds to Ca, where the observed distance between O6* and D1-E189-OE1 is 2.23 Å in the wild-type PSII [13]. At this binding state, the distance between D1-E189-OE1 and the side-chain carbon of D1-V185 is 3.89 Å (PDB code: 8IRF) [13]. Based on this, we speculate that in the D1-T185 conformation-A, where the side-chain carbon of D1-T185 is absent, the flexibility of D1-E189-OE1 will increase (as evidenced by the increase in its B-factor (Supplementary Table 2), as conformation-A provides a larger space for its movement. This space allows a displacement of approximately 1.48 Å for D1-E189-OE2 and OE1. The increased B-factor suggests an increase in the mobility and the instability of D1-E189, which we propose may be associated with the high-spin state observed in the S_2-state.

EPR measurement revealed a higher proportion of a high-spin state in S_2 of the D1-V185T mutant [22] (Fig. 7A). We hypothesize that the high-spin state arises from the D1-V185T-A state, which allows a water molecule to enter into the previously described cavity between Mn1 and O5 (Fig. 7B), thereby enabling a hydrogen bond to form between the water molecule and D1-E189. In the wild-type state, this water molecule insertion would be hindered by D1-V185, as their distance would be approximately 2.8 Å if a water molecule is to be put in the vicinity of D1-V185. Conformation-B of the D1-T185 mutant has a similar distance between its side chain CG1 and the proposed water molecule. On the other hand, the cavity formed by the rotation of D1-T185 in conformation-A provides sufficient space to accommodate OHx (Fig. 7B). This may result in an OHx insertion between Mn1 and O5, as suggested by prior studies [38]. Among various D1-E189 mutants, only D1-E189Q mutant displayed a multiline EPR signal in the S_2 state [39,40], supporting the idea that the high-spin state requires hydrogen bonding between OHx and D1-E189. To accommodate this state, W10 may become unstable, suggesting that the entering water molecule may be W10, which may facilitate the proton release distinct from the low-spin state during the S_1-to-S_2 transition [38].

While no additional changes in the EPR signal were observed beyond the S_2-state, proton release remained delayed in the D1-V185T mutant [22,23]. This delay may be attributed to the significant impact of

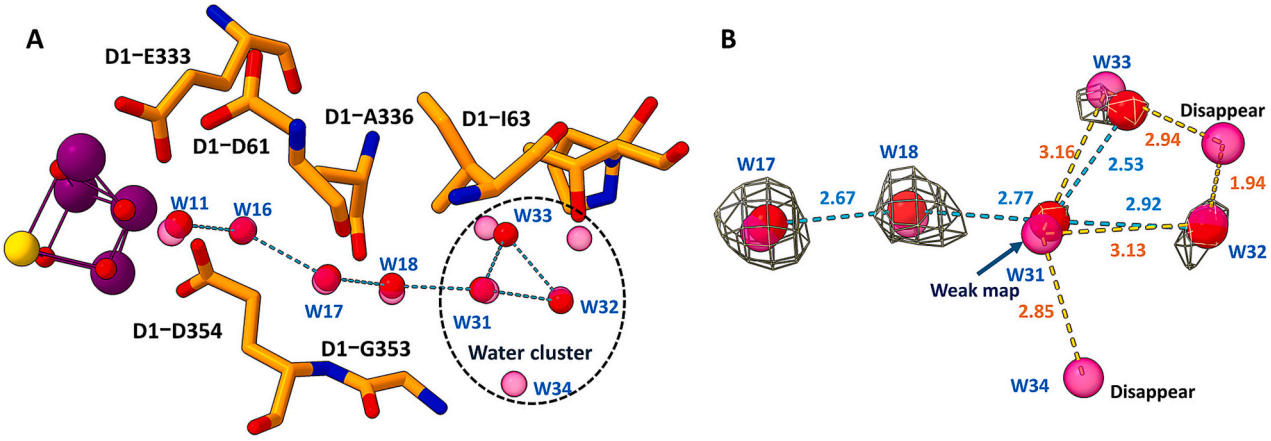

Fig. 6. Movement and disappearance of water molecules in the O4 channel. The water molecules in the O4 channel (A) and an enlarged view of the terminal water molecules (B). The red spheres represent water molecules in the D1-T185 mutant, pink spheres represent water molecules in dark-adapted wild-type structure (8IR5) [13], cyan lines indicate distances between water molecules in the D1-T185 mutant, and yellow lines indicate distances between water molecules in the wild-type structure (8IR5) [13]. The labels shown in blue indicate water molecules. The area circled by a dashed line in panel (A) represents the terminal five water molecules. Disappearance and instability of water molecules in panels A and B are labeled in the figure. (For interpretation of the references to color in this figure legend, the reader is referred to the web version of this article.)

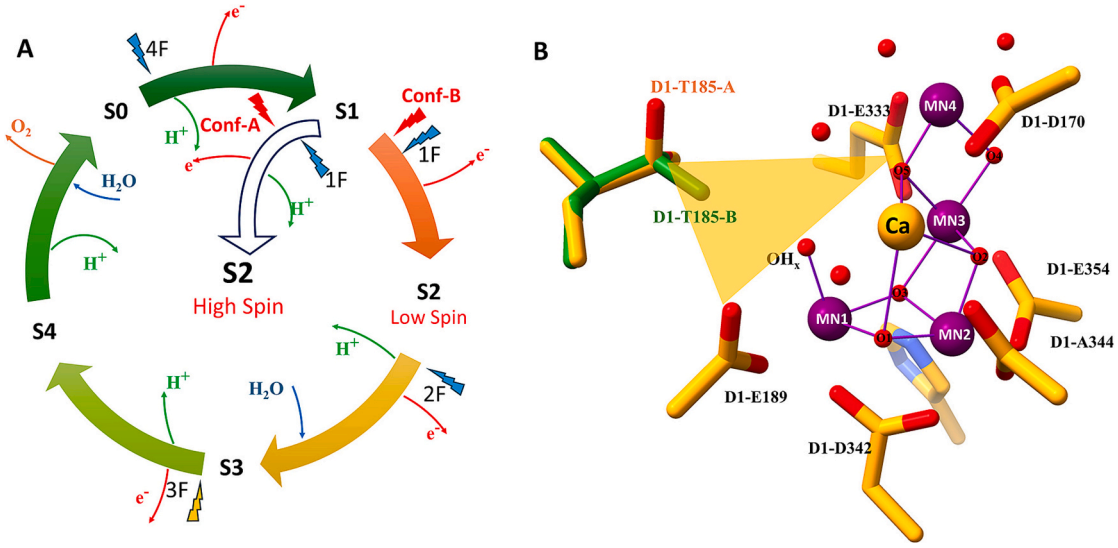

Fig. 7. S-state transitions and the proposed S_2 high-spin form. (A) A schematic illustrating the predicted post-flash S-state conformational transitions for D1-V185T mutant. (B) With the exception of the D1-T185 residue, all coordinates are taken from the S_2 high-spin state, derived from DFT calculations [37]. The D1-T185 residue originates from the mutant structure. The final figure was obtained by fitting the S_2 high-spin state to the mutant structure. Residues shown in green represent the B-conformation of D1-V185T mutant, whereas those in orange represent the A-conformation of the mutant. The transparent orange represents the hydrophilic cavity formed by conformation-A. (For interpretation of the references to color in this figure legend, the reader is referred to the web version of this article.)

conformation-B on the Cl-1 channel. The hydrophilic group of Thr attracts W9, disrupting the hydrogen bond between W9 and W2 and shortening the distance between W9 and the Cl-1 ion. This unusual proximity restricts Cl-1 ion movement, which may potentially interfere with the positive charges on Yz and the OEC during electron transfer.

The disruption of the Cl-1 channel raises uncertainty regarding its continued role in proton transfer. We observed the disappearance of W12 and the appearance of a new water molecule, New-water-2, in the region between D1-D61 and the gate. This suggests a breakdown of the Cl-1 proton channel in conformation-B of the mutant. The increased distance to 3.45 Å between W2 and W1 (Supplementary Table 4) further supports this idea, suggesting that proton transfer may be impeded. Consequently, the O4 channel could serve as an alternative pathway for proton transfer, compensating for the functional loss of the Cl-1 channel in conformation-B (Fig. 6).

Additionally, QM/MM calculations have suggested that oxygen migration during S_4-to-S_0 transition occurs via a cavity formed between D1-V185 and D1-H332 [41]. In conformation-B, the OH^- group of Thr points toward D1-H332, while the absence of the CH_3 group in conformation-A disrupts the hydrophobic environment in this cavity. This disruption might reduce the efficiency of oxygen release and/or prevent the proper expulsion of toxic oxygen species.

Finally, the structure of the D1-V185T mutant solved in this study is compared with the structure of a D1-V185N mutant solved very recently [21]. Both mutants exhibit altered S_2 multiline EPR signal. The D1-V185T mutant displayed two conformations of the substituted T185 residue, whereas the recently reported D1-V185N mutant contained only one conformation of the substituted N185 residue. Nevertheless, both mutants showed conformational heterogeneity of the D2-K317 residue and altered S_2 EPR signals. Due to the differences in the lengths and side chains of the Thr and Gln residues, however, there are some differences in their exact conformations and structures (Fig. 8), although both mutants retain a cavity that may allow accommodation of O6/Ox. These observations provide structural insight into why a hydrophobic residue of D1-V185 is required for proper water oxidation in PSII. Substitution of V185 with a polar residue introduces alternative hydrogen-bonding interactions with nearby water molecules, thereby perturbing the local water network that is critical for OEC function. Some differences in the hydrogen-bond networks are observed between different mutants introduced (Fig. 8). This may bring structural and functional differences observed for the two different mutants. Thus, this study provides another structure for a D1-V185 mutant, and may contribute to our understanding of the detailed mechanism of water oxidation in PSII.

4. Materials and methods

4.1. Mutant construction, cell culture and PSII dimer purification

D1-V185T mutant of the PsbA3-only strain of *T. vestitus*, in which the *psbA*$_1$ and *psbA*$_2$ genes were deleted from the genome, was constructed as described in ref. 22, and was cultivated in a red-light incubator at 45 °C under a photosynthetically active photon flux density (PPDF) of 10 μE photons m^{-2} s^{-1} from a multi-wavelength LED designed for plant growth. Cells were grown in a DTN medium [22,23] supplemented with 0.01 M Na_2HCO_3, and bubbled with a 3% (w/v) CO_2-containing air. The culture was gently stirred using a magnetic stirrer for even distribution. When the culture reached an optical density of $OD_{730} = 1.5$, cells were harvested by centrifugation at 7500 rpm for 20 min at 20 °C, and then flash-frozen in liquid nitrogen and stored at −80 °C for further processing. A small fraction of the cells was used for PCR cloning [22] of the *psbA*$_3$ gene, which was sequenced by Eurofins Genomics Co. (Japan) to confirm the correct point mutation.

For large-scale preparation, frozen cells were thawed with chilled water at 15 °C, and centrifuged at 7500 rpm for 15 min at 4 °C to remove the supernatant. The pellet was resuspended in buffer-1 (1 M betaine, 10% glycerol, 40 mM MES, 15 mM $MgCl_2$, 15 mM $CaCl_2$, pH 6.5 adjusted with NaOH), and centrifuged again at 7500 rpm for 15 min at 4 °C to wash the cells. Next, the cells were resuspended in buffer-1 supplemented with 0.2% (w/v) BSA, 1 mM benzamidine, 1 mM ε-aminocaproic acid, and ~ 50 μg/mL DNase I to a final concentration of 1.5 mg Chl/mL, and disrupted using a French press at 137.9 MPa at 4 °C, with three cycles of breakage. Unbroken cells were removed by centrifugation at 3000 *g* for 5 min at 4 °C, and the supernatant was subjected to ultracentrifugation at 40,000 rpm for 30 min at 4 °C twice, while washing the pellet with buffer-1 each time.

The final pellet was resuspended with a β-dodecyl maltoside (β-DDM)-containing buffer (1 M betaine, 10% glycerol, 40 mM MES, 15

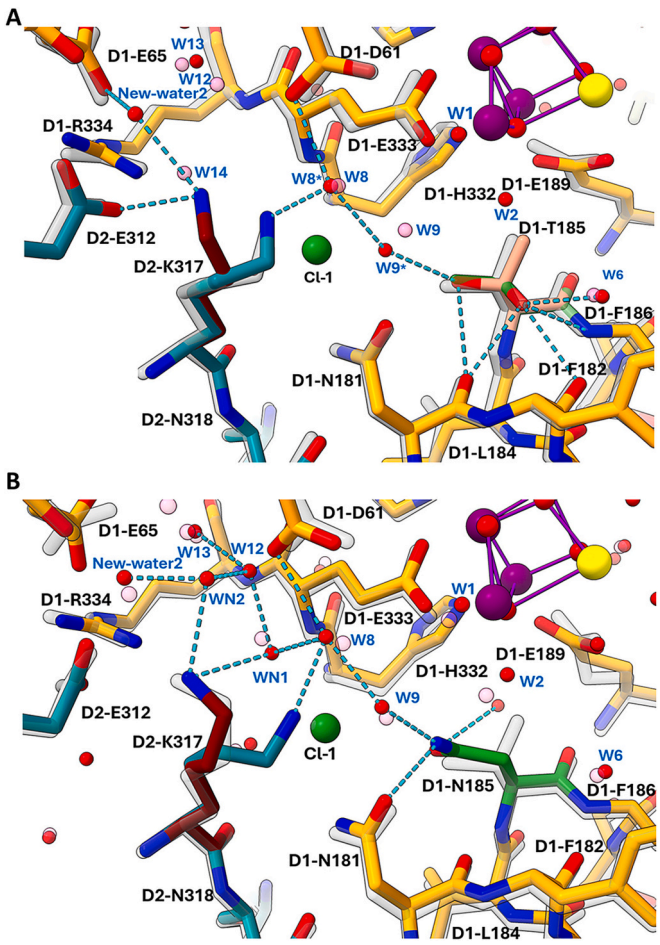

Fig. 8. Structural comparison of the D1-V185T and D1-V185N mutants with the wild-type. (A) Comparison of the wild-type and D1-V185T structures. The D1 protein is shown in orange, and the D2 protein is shown in marine. For D1-T185, the carbon atoms of conformation-A are shown in transparent green, and those of conformation-B are shown in light salmon. All water molecules and oxygen atoms are shown in red, and nitrogen atoms are shown in blue. The wild-type structure with its water molecules shown in transparent pink is from PDB 4UB6 [7]. (B) Comparison of the Synechocystis sp. PCC6803 wild-type and D1-V185N structures. The D1-V185N mutant structure is from PDB 9PHW [21], and the wild-type structure is from PDB 7N8O [56]. (For interpretation of the references to color in this figure legend, the reader is referred to the web version of this article.)

mM $MgCl_2$, 15 mM $CaCl_2$, 0.8% (w/v) n-dodecyl-β-maltoside, 100 mM NaCl, pH 6.5) to a concentration of 1.0 mg Chl/mL and gently mixed for 10 min. The mixture was centrifuged at 40,000 rpm for 20 min at 4 °C to remove any insoluble components. The supernatant was incubated with a pre-equilibrated Ni resin (ProBond resin, Invitrogen, Netherlands) for 2 h at 4 °C, and then loaded into a Bio-Rad econo-column. The flow-through of the column was collected, and the column was washed with buffer-2 (1 M betaine, 10% glycerol, 40 mM MES, 15 mM $MgCl_2$, 15 mM $CaCl_2$, 100 mM NaCl, 0.03% (w/v) β-DDM, pH 6.5) at a flow rate of 0.2 mL/min until the absorbance at 665 nm reached near zero. The column was then eluted with a linear gradient of imidazole from 0 to 500 mM imidazole in buffer-2. The eluted sample was concentrated using an Amicon 100 kDa filter by centrifugation at 5000 rpm for ~30–40 min. The sample was washed 2–3 times with a storage buffer (20 mM MES-NaOH (pH 6.5), 5 mM $CaCl_2$, 0.03% (w/v) β-DDM) to remove residual glycerol and betaine.

Further purification was performed using gel filtration chromatography in a gel filtration buffer (20 mM MES-NaOH (pH 6.5), 50 mM NaCl, 5 mM $CaCl_2$, 0.03% (w/v) β-DDM) to separate PSII dimers and PSII monomers. The dimeric PSII sample was collected and washed with storage buffer and concentrated to 5 mg Chl *a*/mL. The sample was analyzed by clear-native PAGE (CN-PAGE) for dimer content and SDS-PAGE for subunit integrity, and then flash-frozen in liquid nitrogen for storage.

4.2. Measurement of oxygen-evolving activity

The oxygen-evolving activity was measured using a Clark-type oxygen electrode, with phenyl-*p*-benzoquinone and sodium ferricyanide (FeCN) as electron acceptors at 30 °C. The measurement was repeated three times, and the average value was calculated as the oxygen-evolving activity.

4.3. Cryo-EM grid preparation and data collection

Cryo-EM grids were prepared with the Au 300 mesh grids (UltrAuFoil R1.2/1.3) in a Vitrobot chamber in the storage buffer. The grids were rendered hydrophilic prior to utilization using an auto fine coater JEC-3000FC under conditions of 7 Pa, 10 mA for 10 s. The thawed PSII samples were diluted to 2.0 mg Chl *a*/mL, and 3 μL of the sample was applied to the grid. The grid was blotted under 100% humidity with a blot time of 4 s and blot force of 5, then vitrified in liquid ethane. Cryo-EM data were collected by a Krios G4 cryo-EM operated at 300 kV, with magnification and imaging parameters listed in Supplementary Table 1.

4.4. Data processing

Movies consisting of the initial 11 frames each were imported into CryoSPARC [25], and Patch Motion Correction and Patch CTF estimation were performed [42]. A total of 1232 micrographs were used for blob picking, followed by manual inspection and extraction of particles with a box size of 160 pixels. Clean particles were selected through 2D classification, resulting in 18,492 particles. These particles were used as templates for template-based picking, yielding 247,924 particles after iterative selection and 3 rounds of 2D classification.

The particle coordinates were converted to Relion format with CryoSPARC-reoriented Y-axis coordinates and imported into Relion-beta-5.0 [26,43]. Particles were extracted with a box size of 640 pixels and subjected to 3D classification by Relion to refine rotation angles and remove poor-quality particles. Final refinements were performed using Refine 3D [26,44]. Postprocessing, iterative CTF-refine and polish [27] steps were introduced to improve the data quality. Ultimately frames 1–2 were extracted to construct the map and structure with Relion. Reconstruction was conducted using Relion and validated by FSC curve calculations. Local refinement focused on the PsbO region was performed with CryoSPARC, which further improved the resolution to 2.33 Å for the PsbO region (Supplementary Figs. 4, 5). The whole processing workflow is shown in Supplementary Figs. 1, 4 and 5.

4.5. Model building and refinement

The initial model was built based on PDB 7YQ7 [45] and modified using WinCoot-0.9.8.7 [46] at a sigma level of 1.7 rmsd. Regions with poor density were excluded. Local refinements were performed with ServalCat [29] and Phenix Realspace Refine [47,48]. The final model was validated using Phenix validation [49,50] tools, and manual adjustments were made to resolve structural clashes (Supplementary Table 1). The structure was visualized with ChimeraX [51], and water channels were analyzed using MoleOnline [32].

4.6. Conservation analysis of the residue D1-V185 across species

Protein sequences of the D1 protein were first retrieved from UniProt [52] using the search term “gene_exact:psbA”. Non-D1 sequences, including D2 sequences, fragment sequences, and sequences with

abnormal lengths, were removed using SeqKit [53], and only sequences with lengths between 310 and 360 amino acids were retained. Redundant sequences, including identical sequences and duplicate sequences from the same species, were subsequently filtered out, and multiple sequence alignment was performed using MAFFT [54]. A final dataset comprising aligned sequences from 2920 species was obtained, and the conservation at the V185 position was examined and analyzed using Jalview [55].

CRediT authorship contribution statement

Haowei Jiang: Writing – original draft, Visualization, Investigation, Formal analysis, Data curation. **Yoshiki Nakajima:** Validation, Investigation. **Fusamichi Akita:** Investigation, Formal analysis. **Hongjie Li:** Investigation, Formal analysis. **Koji Kato:** Investigation, Formal analysis. **Miwa Sugiura:** Writing – review & editing, Investigation. **Jian-Ren Shen:** Writing – review & editing, Validation, Supervision, Resources, Project administration, Funding acquisition, Conceptualization.

Declaration of competing interest

The authors declare that they do not have any conflicts of interest with the content of this article.

Acknowledgments

This work was supported partially by the Core-Facility Portal (CFPOU) at Okayama University (RIIS-n01), and we thank the International Research Center for Structural Biology of Okayama University for helping collection of the cryo-EM data. This project was supported by JSPS KAKENHI No. JP22H04916 (J.-R.S.), and a JSPS Program for Forming Japan's Peak Research Universities (J-PEAKS) Grant Number JPJS00420230010. MS was supported by a JSPS-KAKENHI grant 24K21853.

Appendix A. Supplementary data

Supplementary data to this article can be found online at https://doi.org/10.1016/j.bbabio.2026.149598.

Data availability

Data will be made available on request.

References

[1] J.-R. Shen, Structure of photosystem II and the mechanism of water oxidation in photosynthesis, Annu. Rev. Plant Biol. 66 (2015) 23–48.
[2] N. Cox, D.A. Pantazis, W. Lubitz, Current understanding of the mechanism of water oxidation in photosystem II and its relation to XFEL data, Annu. Rev. Biochem. 89 (2020) 795–820.
[3] B. Kok, B. Forbush, M. McGloin, Cooperation of charges in photosynthetic O_2 evolution. I. A linear four-step mechanism, Photochem. Photobiol. 11 (1970) 457–475.
[4] E. Schlodder, H.T. Witt, Stoichiometry of proton release from the catalytic center in photosynthetic water oxidation: reexamination by a glass electrode study at pH 5.5–7.2, J. Biol. Chem. 274 (1999) 30387–30392.
[5] H. Suzuki, M. Sugiura, T. Noguchi, Monitoring proton release during photosynthetic water oxidation in photosystem II by means of isotope-edited infrared spectroscopy, J. Am. Chem. Soc. 131 (2009) 7849–7857.
[6] Y. Umena, K. Kawakami, J.-R. Shen, N. Kamiya, Crystal structure of oxygen-evolving photosystem II at a resolution of 1.9 Å, Nature 473 (2011) 55–60.
[7] M. Suga, F. Akita, K. Hirata, G. Ueno, H. Murakami, Y. Nakajima, et al., Native structure of photosystem II at 1.95 Å resolution viewed by femtosecond X-ray pulses, Nature 517 (2015) 99–103.
[8] M. Shoji, H. Isobe, S. Yamanaka, Y. Umena, K. Kawakami, N. Kamiya, et al., Large-scale QM/MM calculations of hydrogen-bonding networks for proton transfer and water inlet channels for water oxidation—theoretical system models of the oxygen-evolving complex of photosystem II, in: Advances in Quantum Chemistry 70, Academic Press, 2015, pp. 325–413.
[9] M. Suga, F. Akita, K. Yamashita, Y. Nakajima, G. Ueno, H. Li, et al., An oxyl/oxo mechanism for oxygen–oxygen coupling in PSII revealed by an X-ray free-electron laser, Science 366 (2019) 334–338.
[10] A. Sirohiwal, D.A. Pantazis, Functional water networks in fully hydrated photosystem II, J. Am. Chem. Soc. 144 (2022) 22035–22050.
[11] M.D. Doyle, A. Bhowmick, D.C. Wych, L. Lassalle, P.S. Simon, J. Holton, et al., Water networks in photosystem II using crystalline molecular dynamics simulations and room-temperature XFEL serial crystallography, J. Am. Chem. Soc. 145 (2023) 14621–14635.
[12] J. Kern, R. Chatterjee, I.D. Young, F.D. Fuller, L. Lassalle, M. Ibrahim, et al., Structures of the intermediates of Kok's photosynthetic water oxidation clock, Nature 563 (2018) 421–425.
[13] H. Li, Y. Nakajima, E. Nango, S. Owada, D. Yamada, K. Hashimoto, et al., Oxygen-evolving photosystem II structures during S1–S2–S3 transitions, Nature 626 (2024) 670–677.
[14] M. Ibrahim, I.D. Young, R. Chatterjee, S. Gul, F.D. Fuller, S. Koroidov, et al., Untangling the sequence of events during the $S_2 \rightarrow S_3$ transition in photosystem II and implications for the water oxidation mechanism, Proc. Natl. Acad. Sci. USA 117 (2020) 12624–12635.
[15] R. Hussein, M. Ibrahim, A. Bhowmick, P.S. Simon, R. Chatterjee, L. Lassalle, et al., Structural dynamics in the water and proton channels of photosystem II during the S2 to S3 transition, Nat. Commun. 12 (2021) 6531.
[16] K. Okamoto, A. Shimada, R. Nagao, H. Akutsu, T. Tomo, T. Noguchi, Proton and water transfer pathways in the $S_2 \rightarrow S_3$ transition of the water-oxidizing complex in photosystem II: time-resolved infrared analysis of the effects of D1-N298A mutation and NO_3^- substitution, J. Phys. Chem. B 125 (2021) 6864–6873.
[17] A. Nakamura, J. Kang, R. Terada, H. Kino, Y. Umena, K. Kawakami, et al., Novel mechanism of Cl-dependent proton dislocation in photosystem II (PSII): hybrid ab initio quantum mechanics/molecular mechanics molecular dynamics simulation, J. Phys. Soc. Jpn. 88 (2019) 084802.
[18] P.L. Dilbeck, H. Bao, C.L. Neveu, R.L. Burnap, Perturbing the water cavity surrounding the manganese cluster by mutating the residue D1-valine 185 has a strong effect on the water oxidation mechanism of photosystem II, Biochemistry 52 (2013) 6824–6833.
[19] C.J. Kim, H. Bao, R.L. Burnap, R.J. Debus, Impact of D1-V185 on the water molecules that facilitate O_2 formation by the catalytic Mn_4CaO_5 cluster in Photosystem II, Biochemistry 57 (2018) 4299–4311.
[20] C. de Lichtenberg, A.P. Avramov, M. Zhang, F. Mamedov, R.L. Burnap, J. Messinger, The D1-V185N mutation alters substrate water exchange by stabilizing alternative structures of the Mn4Ca-cluster in photosystem II, Biochim. Biophys. Acta Bioenerg. 1862 (2021) 148319.
[21] D.A. Flesher, R.J. Debus, G.W. Brudvig, Structure of the D1-Val185Asn mutated photosystem II complex with slow O-O bond formation reveals changes in the Cl1 water channel, Proc. Natl. Acad. Sci. USA 122 (2025) e2522652122.
[22] M. Sugiura, T. Tibiletti, I. Takachi, Y. Hara, S. Kanawaku, J. Sellés, et al., Probing the role of valine 185 of the D1 protein in the photosystem II oxygen evolution, Biochim. Biophys. Acta Bioenerg. 1859 (2018) 1259–1273.
[23] A. Boussac, J. Sellés, T. Tibiletti, M. Sugiura, R.L. Burnap, New insights into the involvement of residue D1/V185 in photosystem II function in *Synechocystis* 6803 and *Thermosynechococcus vestitus*, Biochim. Biophys. Acta Bioenerg. 1866 (2025) 149550.
[24] K. Kato, N. Miyazaki, T. Hamaguchi, Y. Nakajima, F. Akita, K. Yonekura, et al., High-resolution cryo-EM structure of photosystem II reveals damage from high-dose electron beams, Commun. Biol. 4 (2021) 382.
[25] A. Punjani, J.L. Rubinstein, D.J. Fleet, M.A. Brubaker, cryoSPARC: algorithms for rapid unsupervised cryo-EM structure determination, Nat. Methods 14 (2017) 290–296.
[26] S.H.W. Scheres, RELION: implementation of a Bayesian approach to cryo-EM structure determination, J. Struct. Biol. 180 (2012) 519–530.
[27] J. Zivanov, T. Nakane, S.H.W. Scheres, A Bayesian approach to beam-induced motion correction in cryo-EM single-particle analysis, IUCrJ 6 (2019) 5–17.
[28] S. Chen, G. McMullan, A.R. Faruqi, G.N. Murshudov, J.M. Short, S.H.W. Scheres, et al., High-resolution noise substitution to measure overfitting and validate resolution in 3D structure determination by single-particle electron cryomicroscopy, Ultramicroscopy 135 (2013) 24–35.
[29] K. Yamashita, C.M. Palmer, T. Burnley, G.N. Murshudov, Cryo-EM single-particle structure refinement and map calculation using Servalcat, Acta Crystallogr. D Struct. Biol. 77 (2021) 1282–1291.
[30] R. Hussein, A. Graça, J. Forsman, A.O. Aydin, M. Hall, J. Gaetcke, et al., Cryo-electron microscopy reveals hydrogen positions and water networks in photosystem II, Science 384 (2024) 1349–1355.
[31] M. Suga, F. Akita, M. Sugahara, M. Kubo, Y. Nakajima, T. Nakane, et al., Light-induced structural changes and the site of O=O bond formation in PSII caught by XFEL, Nature 543 (2017) 131–135.
[32] L. Pravda, D. Sehnal, D. Toušek, V. Navrátilová, V. Bazgier, K. Berka, et al., MOLEonline: a web-based tool for analyzing channels, tunnels and pores (2018 update), Nucleic Acids Res. 46 (2018) W368–W373.
[33] O. Carugo, Buried chloride stereochemistry in the Protein Data Bank, BMC Struct. Biol. 14 (2014) 19.
[34] K. Saito, A.W. Rutherford, H. Ishikita, Energetics of proton release on the first oxidation step in the water-oxidizing enzyme, Nat. Commun. 6 (2015) 8488.
[35] E. Nogales, S.H.W. Scheres, Single-particle cryo-EM—how did it get here and where will it go, Science 361 (2018) 876–880.
[36] Y. Cheng, N. Grigorieff, P.A. Penczek, T. Walz, A primer to single-particle cryo-electron microscopy, Cell 161 (2015) 438–449.

[37] R. Pokhrel, R.J. Service, R.J. Debus, G.W. Brudvig, Mutation of lysine 317 in the D2 subunit of photosystem II alters chloride binding and proton transport, Biochemistry 52 (2013) 4758–4773.
[38] Y. Pushkar, A.K. Ravari, S.C. Jensen, M. Palenik, Early binding of substrate oxygen is responsible for a spectroscopically distinct S2 state in photosystem II, J. Phys. Chem. Lett. 10 (2019) 5284–5291.
[39] R. Hienerwadel, C. Berthomieu, A.W. Rutherford, Histidine 190-D1 and glutamate 189-D1 provide structural stabilization in photosystem II, Biochemistry 42 (2003) 178–187.
[40] K. Saito, A.W. Rutherford, H. Ishikita, Roles of D1-Glu189 and D1-Glu329 in O_2 formation by the water-splitting Mn_4Ca cluster in photosystem II, Biochemistry 59 (2020) 4365–4374.
[41] M. Retegan, D.A. Pantazis, Concerted mechanism of water insertion and O_2 release during the S4 to S0 transition of the oxygen-evolving complex in photosystem II, J. Phys. Chem. B 122 (2018) 8312–8321.
[42] K. Zhang, Gctf: real-time CTF determination and correction, J. Struct. Biol. 193 (2016) 1–12.
[43] D. Kimanius, K. Jamali, M.E. Wilkinson, S. Lövestam, V. Velazhahan, T. Nakane, et al., Data-driven regularization lowers the size barrier of cryo-EM structure determination, Nat. Methods 21 (2024) 1216–1221.
[44] S.H.W. Scheres, S. Chen, Prevention of overfitting in cryo-EM structure determination, Nat. Methods 9 (2012) 853–854.
[45] Y. Nakajima, N. Ugai-Amo, N. Tone, A. Nakagawa, M. Iwai, M. Ikeuchi, et al., Crystal structures of photosystem II from a cyanobacterium expressing *psbA2* in comparison to *psbA3* reveal differences in the D1 subunit, J. Biol. Chem. 298 (2022) 102668.
[46] P. Emsley, K. Cowtan, Coot: model-building tools for molecular graphics, Acta Crystallogr. D Biol. Crystallogr. 60 (2004) 2126–2132.
[47] P.D. Adams, P.V. Afonine, G. Bunkóczi, V.B. Chen, I.W. Davis, N. Echols, et al., PHENIX: a comprehensive Python-based system for macromolecular structure solution, Acta Crystallogr. D Biol. Crystallogr. 66 (2010) 213–221.
[48] P.V. Afonine, R.W. Grosse-Kunstleve, N. Echols, J.J. Headd, N.W. Moriarty, M. Mustyakimov, et al., Towards automated crystallographic structure refinement with phenix.refine, Acta Crystallogr. D Biol. Crystallogr. 68 (2012) 352–367.
[49] L. Urzhumtseva, P.V. Afonine, P.D. Adams, A. Urzhumtsev, Crystallographic model quality at a glance, Acta Crystallogr. D Biol. Crystallogr. 65 (2009) 297–300.
[50] C.J. Williams, J.J. Headd, N.W. Moriarty, M.G. Prisant, L.L. Videau, L.N. Deis, et al., MolProbity: more and better reference data for improved all-atom structure validation, Protein Sci. 27 (2018) 293–315.
[51] E.C. Meng, T.D. Goddard, E.F. Pettersen, G.S. Couch, Z.J. Pearson, J.H. Morris, et al., UCSF ChimeraX: tools for structure building and analysis, Protein Sci. 32 (2023) e4792.
[52] The UniProt Consortium, UniProt: the universal protein knowledgebase in 2025, Nucleic Acids Res. 53 (D1) (2024) D609–D617.
[53] W. Shen, S. Le, Y. Li, F. Hu, SeqKit: a cross-platform and ultrafast toolkit for FASTA/Q file manipulation, PLoS One 11 (2016) e0163962.
[54] K. Katoh, K. Misawa, K. Kuma, T. Miyata, MAFFT: a novel method for rapid multiple sequence alignment based on fast Fourier transform, Nucleic Acids Res. 30 (2002) 3059–3066.
[55] A.M. Waterhouse, J.B. Procter, D.M.A. Martin, M. Clamp, G.J. Barton, Jalview version 2 - a multiple sequence alignment editor and analysis workbench, Bioinformatics 25 (2009) 1189–1191.
[56] C.J. Gisriel, J. Wang, J. Liu, D.A. Flesher, K.M. Reiss, H. Huang, et al., High-resolution cryo-electron microscopy structure of photosystem II from the mesophilic cyanobacterium, *Synechocystis* sp. PCC 6803, Proc. Natl. Acad. Sci. USA 119 (2022) e2116765118.